Advanced Electronic Materials

ADVANCED ELECTRONIC MATERIALS Open Access

www.advelectronicmat.de

RESEARCH ARTICLE OPEN ACCESS

XHEMTs on Ultrawide Bandgap Single-Crystal AlN Substrates

Eungkyun Kim[1] | Yu-Hsin Chen[2] | Naomi Pieczulewski[2] | Jimy Encomendero[1] | David Anthony Muller[3,4] | Debdeep Jena[1,2,4] | Huili Grace Xing[1,2,4]

[1]School of Electrical and Computer Engineering, Cornell University, Ithaca, New York, USA | [2]Department of Materials Science and Engineering, Cornell University, Ithaca, New York, USA | [3]School of Applied and Engineering Physics, Cornell University, Ithaca, New York, USA | [4]Kavli Institute at Cornell for Nanoscale Science, Cornell University, Ithaca, New York, USA

Correspondence: Eungkyun Kim (ek543@cornell.edu) | Debdeep Jena (djena@cornell.edu) | Huili Grace Xing (grace.xing@cornell.edu)

Received: 14 June 2025 | **Revised:** 8 November 2025 | **Accepted:** 11 November 2025

Keywords: AlN | GaN | HEMT | homoepitaxy | single crystal | wide-bandgap

ABSTRACT

AlN has the largest bandgap in the wurtzite III-nitride semiconductor family, making it an ideal barrier for a thin GaN channel to achieve strong carrier confinement in field-effect transistors, analogous to silicon-on-insulator technology. Unlike SiO_2/Si/SiO_2, AlN/GaN/AlN can be grown fully epitaxially, enabling high carrier mobilities suitable for high-frequency applications. However, developing these heterostructures and related devices has been hindered by challenges in strain management, polarization effects, defect control, and charge trapping. Here, the AlN single-crystal high electron mobility transistor (XHEMT) is introduced, a new nitride transistor technology designed to address these issues. The XHEMT structure features a pseudomorphic GaN channel sandwiched between AlN layers, grown on single-crystal AlN substrates. XHEMTs demonstrate RF performance on par with the state-of-the-art GaN HEMTs, achieving 5.92 W/mm output power and 65% peak power-added efficiency at 10 GHz under 17 V drain bias. These devices overcome several limitations present in conventional GaN HEMTs, which are grown on lattice-mismatched foreign substrates that introduce undesirable dislocations and exacerbated thermal resistance. With the recent availability of 100-mm AlN substrates and AlN's high thermal conductivity (340 W/m · K), XHEMTs show strong potential for next-generation RF electronics.

1 | Introduction

Often the development of new crystals creates entirely new fields, and simultaneously rejuvenates the existing state of the art. High quality single-crystal wafers of the ultrawide bandgap semiconductor aluminum nitride (AlN) up to 100 mm diameter in size have recently become possible [1, 2]. Such substrates are unleashing a new era of UV photonics by enabling the first ever electrically injected continuous wave deep-UV semiconductor diode lasers [3]. AlN has a direct energy bandgap > 6 eV, an ultrahigh natural electrical resistivity of $\rho_{300K} \approx 10^{14}\ \Omega \cdot \text{cm}$, and a high thermal conductivity of $\kappa_{300K} \approx 340\ \text{W/m} \cdot \text{K}$ [see Figure 1(a)] [4]. This combination is a 'dream list' of desirable properties of ultrawide bandgap semiconductor substrates for next generation high speed microwave transistors for electronics, provided high electrical conductivity channels can be created and modulated with a gate voltage efficiently.

To add to the above physical properties, the AlN crystal has a wurtzite lattice structure that exhibits broken inversion symmetry along the $c-$axis. This broken symmetry produces large spontaneous and piezoeletric polarization, a physical property that is absent in other ultrawide bandgap semiconductors such as diamond and $\beta - Ga_2O_3$. The change in polarization across

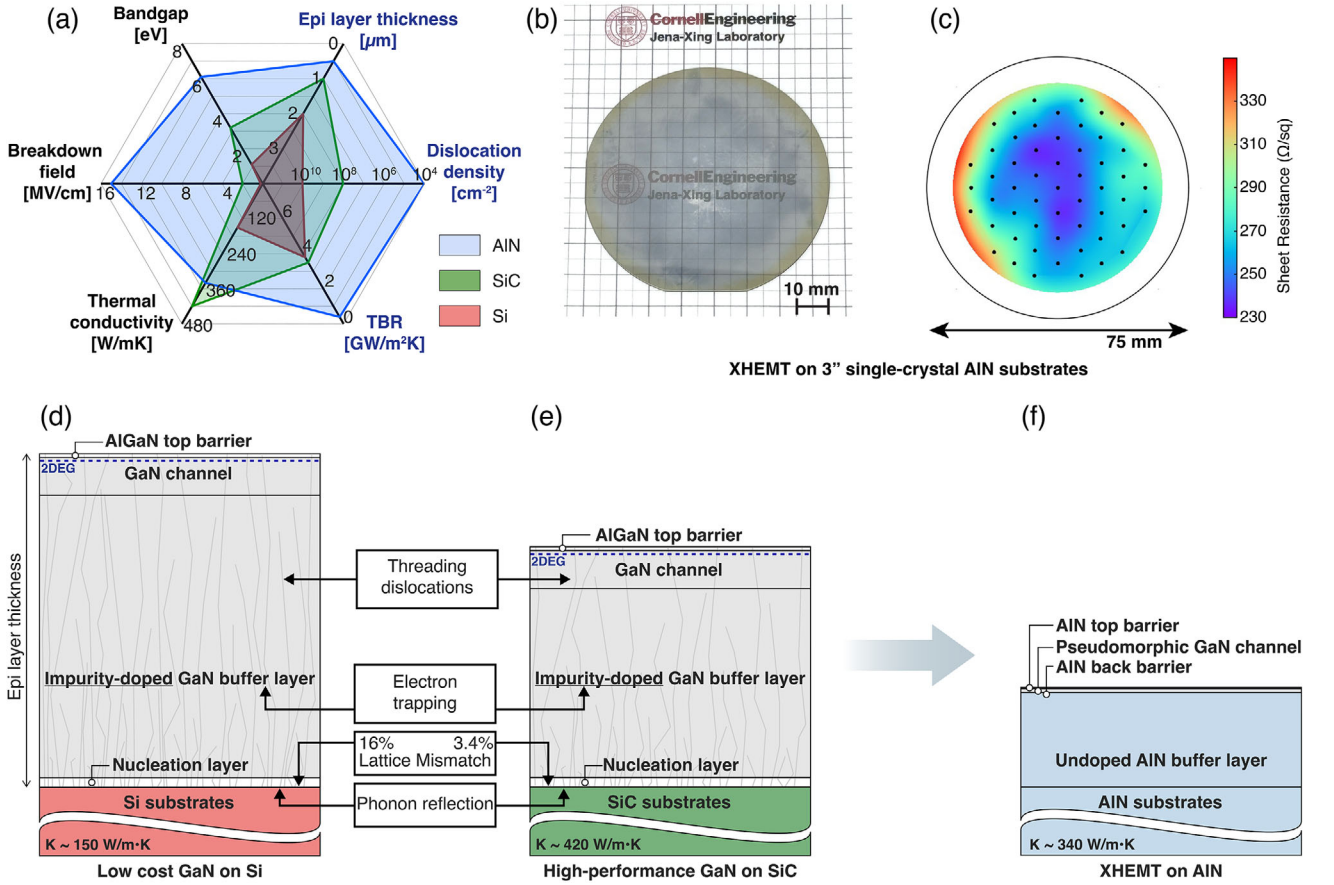

FIGURE 1 | A tale of three substrates for nitride HEMTs. (a) Spider plot comparing the key material properties of substrates and device epitaxy used in GaN HEMTs. The AlN/GaN/AlN XHEMT platform promises to take advantage of AlN's unique combination of an ultrawide bandgap and high thermal conductivity. More importantly, pseudomorphic epitaxy of ultra-thin GaN channel on single crystal AlN leads to very low dislocation densities (determined by the substrate, about 10^4 cm^{-2}) and nearly zero thermal boundary resistance. (b) Optical image and (c) sheet resistance map of the AlN/GaN/AlN XHEMT grown on 3-inch single-crystal AlN substrates. The Cornell University emblem is used with permission. Representative layer structures of commercially available GaN HEMTs on (d) Si substrates for cost-effectiveness and (e) SiC substrates for high-performance. Both are affected by electron trapping in the buffer layer, high dislocation densities (about 10^9 cm^{-2}), and a high thermal boundary resistance (TBR) arising from heteroepitaxy, which also necessitates much thicker epitaxial buffer layers. These challenges are more pronounced in Si substrates due to their lower thermal conductivity, larger lattice and phonon mismatch with GaN. (f) The XHEMT structure addresses these issues by offering zero lattice and phonon mismatch at the growth interface on the substrate, ultra-thin channel with large electron confinement, and high thermal conductivity and high electrical resistivity of AlN.

junctions has enabled the formation of high mobility two-dimensional electron gases (2DEGs) [5–7] and two-dimensional hole gases (2DHGs) [8] at undoped quantum well (QW) heterojunctions of AlN and GaN grown on single-crystal AlN substrates with nearly million times lower dislocation densities than conventional templates such as AlN on silicon or SiC.

Can the newly available large-area bulk AlN substrate platform rejuvenate nitride electronics? In this work we show how a new device structure called the XHEMT—for single-crystal (Xtal) high electron mobility transistor—exploits the unique properties of the high quality single-crystal AlN bulk substrate to provide a path to overcome several hurdles faced in today's nitride transistors. AlN XHEMTs are a subset of pseudomorphic AlN/GaN/AlN HEMTs (AlN pHEMTs) since AlN XHEMTs employ bulk AlN substrates while AlN pHEMTs employ any suitable substrates. We also explicitly point out the challenges that need to be overcome for the XHEMT in the near future. By overcoming some hurdles, we demonstrate that XHEMTs deliver high currents, output powers of ~6 W/mm, and 65% power added efficiency in the X-Band, establishing it as a new nitride transistor technology. The new XHEMT architecture enables a number of new possibilities that are not attainable in current AlGaN/GaN HEMTs, and thus offers an exciting future for nitride electronics.

Figure 1b shows an example 75 mm single-crystal Al-polar AlN bulk substrate wafer, on which we perform homoepitaxy of AlN and then insert a 20 nm coherently strained GaN QW to obtain a high conductivity 2DEG channel due to the polarization discontinuity. The sheet resistance of the 2DEG channel is in the ~ 250 Ω/□ range with the inhomogeneity indicated in Figure 1c. We subsequently use this epiwafer to fabricate XHEMTs. Before describing the process, we discuss the details of the formation of the conductive 2DEG and how it is different from the conventional AlGaN/GaN geometry used today.

Figure 1d shows the cross section of conventional AlGaN/GaN HEMTs developed on Si primarily for power electronics [9], and Figure 1e shows that of AlGaN/GaN HEMTs on SiC used for radio frequency (RF) power amplifiers [10, 11]. HEMTs on silicon offer a low-cost option, but do require a thick GaN epitaxial layer to obtain high GaN crystalline quality by reduction of dislocation density by annihilation, and to keep the narrower bandgap silicon far from high electric field regions. The nearly 17% lattice mismatch between GaN and Si, along with their thermal expansion coefficient mismatch therefore tensile strain induced during post-growth wafer cooling, leads to wafer curvature, cracking, and defect formation, which require several buffer layers and defect mitigation schemes developed in the past decades [12, 13]. The undesired mobile n-type carriers due to unintentional shallow donor impurities in the thick GaN buffer layer is compensated by Fe or C impurity doping that introduce deep levels inside the energy bandgap of GaN [14, 15]. The high defect density and thermal boundary resistance at the nucleation layer/silicon interface introduce a bottleneck in heat dissipation, which has been recognized as a fundamental factor preventing AlGaN/GaN HEMTs from approaching their theoretical output-power limit [16, 17]. Although not explicitly shown in Figure 1, sapphire is another commonly used low-cost substrate, exhibiting similar issues due to its ~14% lattice mismatch with GaN and its even-lower-than-Si thermal conductivity.

Because the lattice mismatch between GaN and SiC is 3.4%, smaller than that between GaN and Si, and SiC has a high thermal conductivity and larger bandgap than silicon, thinner epitaxial layers and better heat dissipation is obtained in AlGaN/GaN HEMTs on SiC. The thinner epitaxial layers cause lower wafer curvature, though the dislocation density is still typically $\sim 10^9/\text{cm}^2$ even in the best GaN HEMTs on SiC that are currently favored for high power microwave power amplifiers. The thermal boundary resistance between the nitride and SiC layer remains a concern [18].

Figure 1f shows the layer structure of the XHEMT on single-crystal AlN. The epitaxial layer thickness is dramatically reduced by 2X to 4X and potentially more compared to growths on silicon or SiC. The AlN homoepitaxial layer grown on AlN eliminates three critical limitations: (1) dislocations through coherent epitaxy [19], (2) the need for deep level compensation dopants because undoped AlN has ultrahigh resistivity and low RF loss [20], and (3) thermal boundary resistance at the epi-substrate interface [21]. Placing a thin pseudomorphic GaN channel directly on high-thermal-conductivity homoepitaxial AlN brings the device hot spot closer to the AlN heat sink, enabling significantly more efficient heat management. A detailed thermal analysis of XHEMTs on AlN will be presented in a separate publication. An AlN barrier grown on a pseudomorphic GaN channel experiences nearly zero strain and can therefore be made arbitrarily thick, providing flexible control of the 2DEG density. In contrast, a high-Al-content AlGaN barrier on relaxed GaN faces strain-management challenges [22]. The high 2DEG density attainable in such XHEMT heterostructures may offer improved impedance-matching bandwidth, comparable to other barrier technologies that support similarly large 2DEG densities, including ternary AlScN and quaternary InAlGaN barriers [23, 24].

The choice of AlN substrates not only affects the crystal quality and the electrical and thermal properties of the transistor, but also drastically alters the charge distribution within the heterostructure. Just as the polarization discontinuity at the Al(Ga)N/GaN interface induces the desired 2DEG, the polarization charge at the AlN/GaN interface, now with the opposite sign, induces 2DHG as reported in our earlier studies [25, 26]. Therefore, unlike the conventional HEMT structures shown in Figure 1d,e, the 2DEG and 2DHG are expected to coexist in the thin GaN channel layer of the XHEMT structure. In this study, we find that the 2DHG, located approximately 18 nm below the electron channel, causes severe charge trapping effects during RF operation and limit the transistor's output power and efficiency. We further show that inserting a sheet of silicon donors can effectively compensate the 2DHG and eliminate its adverse effects on RF performance while simultaneously boosting the 2DEG conductivity.

2 | Results and Discussion

2.1 | Heterostructure Design and Electrical Transport Characteristics

Undoped and silicon δ-doped XHEMTs are compared in Figure 2 in terms of their layer structures, equilibrium energy band diagrams and charge distributions, and capacitance–voltage (C–V) characteristics. Figure 2a illustrates the epitaxial heterostructure of the undoped XHEMT. The structure consists of a 500 nm homoepitaxial AlN buffer layer grown on single-crystal metal-polar AlN substrates from Asahi-Kasei Corporation [2, 3], a 20 nm coherently strained GaN channel, and a 6 nm AlN top barrier capped with a 1 nm GaN layer. The reciprocal space mapping (RSM) around the asymmetric (−105) diffraction peak yielded $a-$ and $c-$ lattice parameters of 3.11 Å and 5.24 Å of the strained GaN layer, confirming the pseudomorphic growth of the GaN channel layer. This is further corroborated by transmission electron microscopy (TEM) imaging, showing no additional dislocations generated in the pseudomorphic GaN channel: undoped as well as δ-doped. Detailed structural characterizations by X-Ray Diffraction (XRD) of undoped and δ-doped XHEMTs can be found in our recent publications [6, 27]. The growth conditions of XHEMTs presented in this study can be found in the Experimental Section of this paper.

Hall-effect measurements at room temperature performed on as-grown samples revealed a 2DEG of density and electron mobility of 1.80×10^{13} cm^{-2} and 717 cm^2/V · s, corresponding to a sheet resistance of 485 Ω/□ in undoped XHEMT, and 3.16×10^{13} cm^{-2} and 644 cm^2/V · s, corresponding to a sheet resistance of 307 Ω/□ in δ-doped XHEMT, respectively. The increase in the 2DEG density in the δ-doped XHEMT structure, owing to silicon δ-doping, leads to a ~ 36.8% reduction in sheet resistance. In a more recently grown δ-doped XHEMT sample with further growth optimization, although devices have not yet been fabricated, a 2DEG density of 3.21×10^{13} cm^{-2} and electron mobility of 855 cm^2/V · s, corresponding to a sheet resistance of 227 Ω/□ were measured, resulting in a ~ 53.1% reduction in sheet resistance compared to the undoped XHEMT. Details of the epitaxial growth and temperature-dependent transport studies are provided in Reference [6].

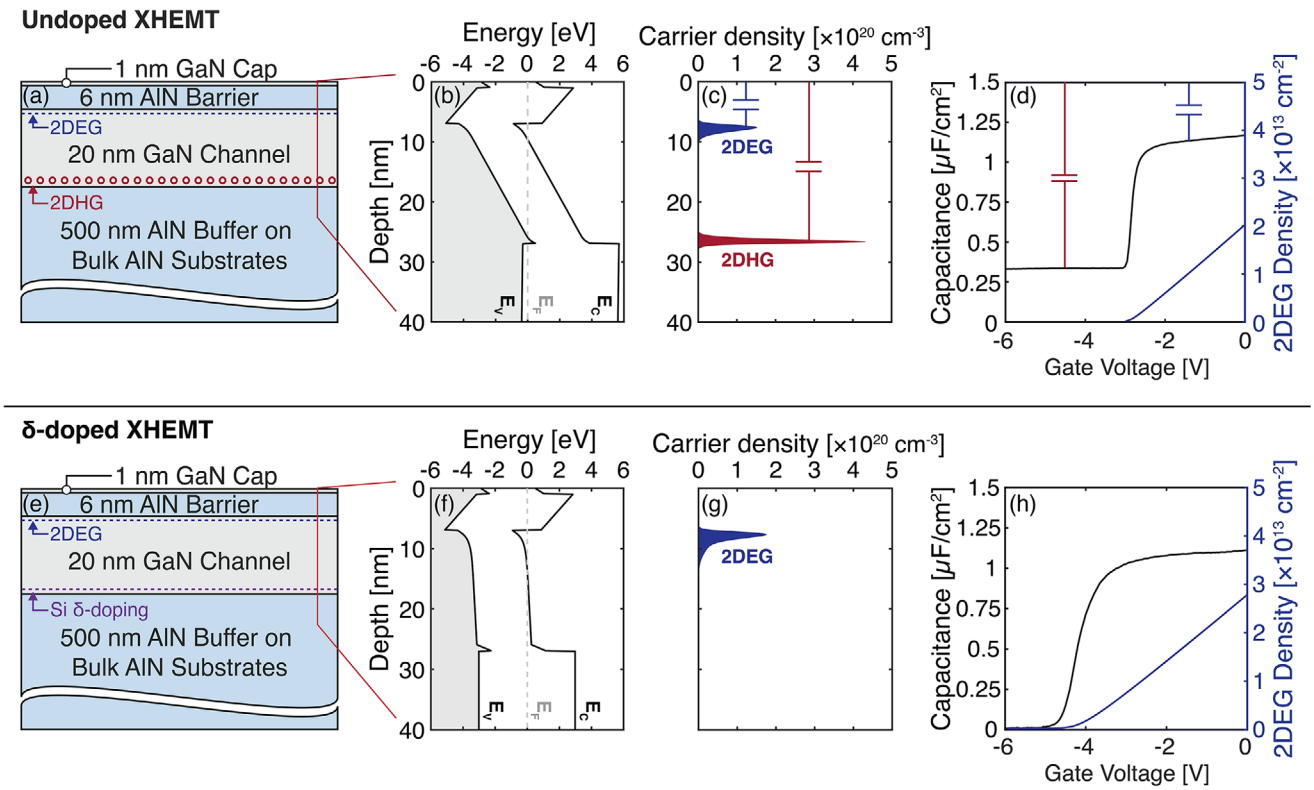

FIGURE 2 | Undoped XHEMT (top row) vs δ-doped XHEMTs (bottom row) on AlN. Layer structure of the (a) undoped XHEMT and (e) δ-doped XHEMT in this study, both consisting of epitaxial AlN/GaN/AlN layers on bulk AlN. δ-doped XHEMT uniquely refers to the structure with silicon δ-doping thus only the electron channel is present. Otherwise, the two structures are nominally the same. Simulated energy band diagrams of (b) undoped XHEMT and (f) δ-doped XHEMT. Silicon donors compensate for the net negative polarization charge at the bottom GaN/AlN interface on metal-polar AlN, shifting the Fermi level in GaN away from the valence band and closer to the midgap of AlN back barrier in δ-doped XHEMT. This results in a reduction of the average vertical electric field in GaN experienced by the 2DEG. Simulated carrier density profile of (c) undoped and (g) δ-doped XHEMT. Silicon δ-doping prevents accumulation of 2DHG at the bottom GaN/AlN interface and increases the 2DEG density in the channel by modulation doping effect. (d) C–V characteristics of the undoped XHEMT. Two plateaus are observed, corresponding to the 2DEG and the 2DHG present in the device structure as indicated by the color-coded capacitor symbols, respectively. (h) C-V characteristics of the δ-doped XHEMT, confirming single electron channel operation.

Figure 2b,c shows the simulated energy band diagram and carrier density profile, respectively, using boundary conditions of a 0.5 eV surface barrier height, an UID AlN buffer, and a Fermi level pinned at midgap in the AlN substrate. The band diagrams over the full simulated depth are presented in Figure S1. In addition to the polarization-induced 2DEG at the top AlN/GaN interface, the calculations suggest that net negative polarization bound charges at the bottom GaN/AlN interface induce positive mobile charges with a large density of $p_s \sim 3.9 \times 10^{13}$ cm^{-2}, confined by the valence band offset between GaN and AlN. The existence of the positive charges at this GaN/AlN interface was investigated by the C-V measurement performed on on-wafer circular Schottky diodes. As shown in Figure 2d, a second capacitance plateau is observed beyond the 2DEG depletion, corresponding to a mobile sheet charge situated near the bottom GaN/AlN interface, indicated by the capacitor symbol in red. The capacitance at this second plateau is 0.34 μF/cm^2, corresponding to a depth of 26 nm below the surface where the positive charges are expected based on the simulation results. The appearance of this second plateau is unexpected, as no intentional contacts to the 2DHG were made. We believe the contact is established partly through capacitive coupling under AC excitation and partly through tunneling across the n+ GaN/2DHG interface under DC bias with a resistance higher than 10 k$\Omega \cdot$ mm but low enough for us to observe the second plateau in the C–V measurement.

We attribute this second plateau to the presence of a 2DHG, supported by two other independent observations in XHEMT-like heterostructures. In undoped GaN/AlN heterostructures on single-crystal AlN substrates using the same growth conditions, i.e., undoped XHEMT structures without the top barrier layers, we consistently observe high-density 2DHGs [8, 26]. In fact, in these 2DHGs we have recently achieved the highest hole mobilities [28], which in turn enabled us to observe quantum oscillations of light and heavy holes in GaN for the first time [25] since p-type GaN was invented in 1989 by Amano et al. [29]. In another undoped 3-nm AlN/10-nm GaN/AlN heterostructure, we observe the presence of a 2DHG in as-grown samples by Hall effect measurements but not 2DEG due to the thinner GaN channel; the detailed results will be published in a separate study. In Figure S2, we present the frequency-dependent C–V data, the extracted carrier concentration as a function of depth, and the measured complex-impedance data of the undoped XHEMTs in this study. While these three independent evidences suggest the presence of a 2DHG in the undoped AlN XHEMT on

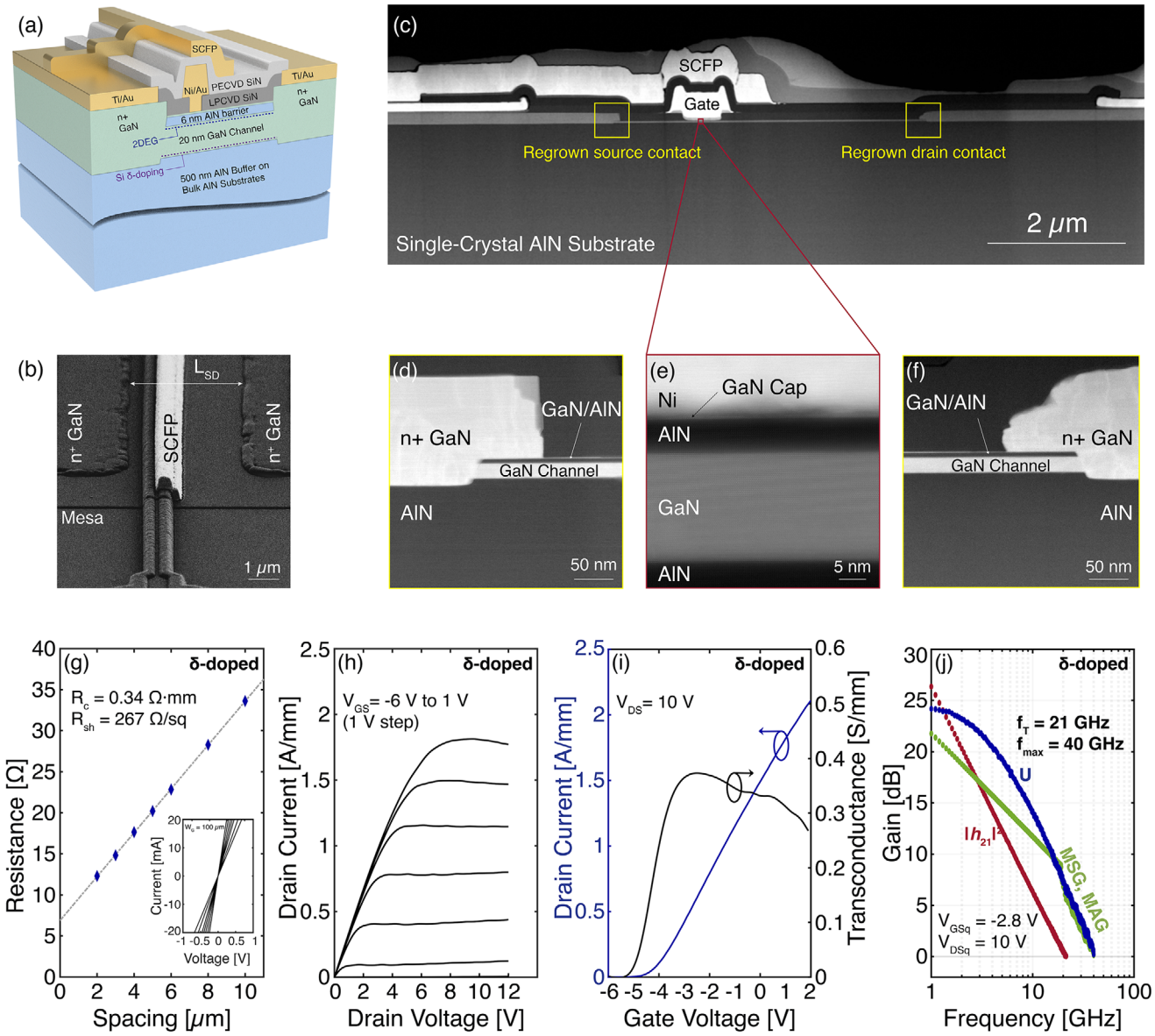

FIGURE 3 | δ-doped XHEMT. (a) Three-dimensional representation and (b) SEM image of a fully fabricated δ-doped XHEMT. (c) Cross-sectional STEM image showing the regrown source and drain contacts, a T-shaped gate, and a source-connected field plate. The cross-sectional images were taken along the plane that intersects the bridge connecting the field plate to the source pad. (d) Magnified STEM image showing the regrown GaN/2DEG interface on the source side. (e) Atomic-resolution HAADF-STEM image revealing a sharp heterojunction with a coherently strained GaN channel layer under the gate. (f) Magnified STEM image showing the regrown GaN/2DEG interface on the drain side. Threading dislocations are widely observed within the relaxed regrown n+ GaN, but not seen in the pseudomorphically strained GaN channel of the δ-doped XHEMT. (g) Linear TLM analysis performed on δ-doped XHEMTs, showing a contact resistance $R_c = 0.34\ \Omega \cdot$ mm between the ohmic metal and the 2DEG and a 2DEG sheet resistance $R_{sh} = 267\ \Omega/\square$. (h) Linear plot showing the family of I–V curves for a δ-doped XHEMT with a gate-to-source voltage ranging from −6 V to 2 V in steps of 1 V. (i) Drain current (blue line) and transconductance (black line) of a δ-doped XHEMT as a function of gate-to-source voltage, operating at a drain-to-source voltage of 10 V. (j) Semi-log plot showing the small-signal current gain (red line), unilateral gain (blue line), and maximum stable and available gain (green line). A δ-doped XHEMT biased at a gate-to-source voltage $V_{GSq} = -2.8$ V and a drain-to-source voltage $V_{DSq} = 10$ V revealed $f_T/f_{max} =$ 21/40 GHz. The extra parasitic delays introduced by device probe pads were not de-embedded. The dimensions of the measured δ-doped XHEMTs are $L_G = 0.45\ \mu$m, $L_{SD} = 4.5\ \mu$m, $L_{GD} = 3.05\ \mu$m, and $W_G = 2 \times 100\ \mu$m.

metal-polar AlN, additional verification—such as gated Hall-effect measurements—would further confirm the 2DHG presence.

The influence of the 2DHG on electrical characteristics of undoped XHEMTs remained largely unexplored to date. To investigate the effect of the uncompensated positive charges at the GaN/AlN interface, we performed identical growths, differing only by the introduction of silicon δ-doping with a donor density of 5×10^{13} cm^{-2}, inserted 1 nm above the bottom GaN/AlN interface, as shown in Figure 2e. In this δ-doped XHEMT structure, the additional electrons supplied by the silicon donors compensate for the positive charges, shifting the valence band away from the Fermi level. The compensation provided by the silicon donors

reduces the polarization effect at the GaN/AlN interface, thereby lowering the vertical electric field in the GaN QW and pushing the centroid of the electron wave function further away from the interface. This redistribution of electron wave function results in reduced interface roughness scattering, enhancing electron mobility. The remaining electrons, after compensation, increases the 2DEG density through the modulation doping effect, as they migrate to the opposite end of the QW and become confined. Hence, a concurrent increase in both electron mobility and 2DEG density is expected with silicon δ-doping. The simulated energy band diagram and carrier density profile, shown in Figure 2f,g, show the anticipated suppression of positive charges and the reduction of the average vertical field in the GaN QW. The carrier density-weighted average field in GaN QW is 2.84 MV/cm in δ-doped XHEMTs and 3.80 MV/cm in undoped XHEMTs, respectively, calculated as $F_{avg} = \frac{\int n(z)F(z)dz}{\int n(z)dz}$, where $n(z)$ is the local electron density and $F(z)$ is the local electric field along the direction z perpendicular to the sample surface. The C–V characteristics of a δ-doped XHEMT, as shown in Figure 2h, confirm the charge compensation, showing a C–V profile closely aligned with the expected behavior of a GaN HEMT with a single electron channel with no 2DHG: the capacitance sharply decreases at the threshold voltage as the 2DEG is depleted and no additional plateau is observed.

2.2 | Device Design, DC Performance, and Small-Signal RF Characteristics

Fully fabricated δ-doped XHEMTs are shown schematically in Figure 3a. The source and drain ohmic contacts were formed by exposing the 2DEG sidewall with an inductively coupled plasma (ICP) etch that extended approximately 10 nm into the AlN buffer layer, followed by regrowth of a heavily silicon doped n+ GaN layer by MBE. The devices were passivated with a 106-nm thick near stoichiometric silicon nitride (SiN_x) layer deposited by low pressure chemical vapor deposition (LPCVD). A nickel/gold metal stack was used to form the Schottky gate contact, and a source-connected field plate (SCFP) was implemented, separated from the gate metal by a 118 nm thick silicon nitride layer deposited by plasma-enhanced chemical vapor deposition (PECVD). A scanning electron microscope (SEM) image of a fully processed δ-doped XHEMT, taken at a 70-degree angle, is shown in Figure 3b. The undoped XHEMTs were fabricated using the same process flow. Details of the device fabrication can be found in the experimental section.

The high-resolution cross-sectional scanning transmission electron microscopy (STEM) image (Figure 3c) shows the device cross-section, featuring a gate length (L_G) of 0.45 μm, a source-to-drain distance (L_{SD}) of 4.5 μm, and a gate-to-drain distance (L_{GD}) of 3.05 μm. As depicted in the device schematic in Figure 3a, SCFPs are connected to the source pad via a 5-μm-wide bridge covering the access region over a device width (W_G) of 100 μm to minimize parasitic gate-to-source capacitance. Cross-sectional images were taken along the plane intersecting this bridge. Figure 3d,f shows the source and drain ohmic contacts, respectively, formed with a regrown n++ GaN layer. To ensure intimate regrown contacts, the ICP etch parameters were selected to expose the 2DEG sidewall at a 50-degree angle with respect to the epitaxial interface, with the regrown n++ GaN layer extending 80 nm into the access region. The atomic-resolution STEM image in Figure 3e, taken under the T-shaped gate, revealed atomically sharp interfaces. To facilitate easier viewing of atomic details, a larger version of the STEM image is provided in Figure S3. Unless otherwise specified, the device dimensions are identical across DC, small-signal, and large-signal measurements shown in this study.

Following device fabrication, the contact resistance (R_c) and sheet resistance (R_{sh}) were extracted using the linear transfer length method (TLM), as shown in Figure 3g. An average R_c of 0.39 $\pm$ 0.04 $\Omega \cdot$ mm and R_{sh} of 276 $\pm$ 9.5 $\Omega/\square$ were obtained from multiple TLM measurements across the sample. The extracted R_{sh} closely aligns with the R_{sh} of 283 $\Omega/\square$ obtained by the Hall effect measurement on an on-wafer van der Pauw pattern post-device fabrication. The lower R_{sh}, compared to the value measured on the as-grown sample prior to device fabrication, is attributed to the increased 2DEG density due to surface passivation with LPCVD SiN_x.

Figure 3h shows the representative output characteristics of δ-doped XHEMTs. At room temperature, the device exhibits a maximum drain current density exceeding 2 A/mm at a gate voltage of 2 V. This high drain current density is realized without aggressive lateral scaling of the device, owing to the enhanced 2DEG density provided by the AlN barrier and silicon δ-doping. Figure 3i shows the transfer characteristics of the δ-doped XHEMTs. At a fixed drain voltage of 10 V, a threshold voltage of −4.2 V, linearly extrapolated from the transfer characteristics, and a peak extrinsic transconductance exceeding 0.37 S/mm were extracted. Figure 3j shows the small-signal unilateral gain (U), current gain ($|h_{21}|^2$), maximum stable gain (MSG), and maximum available gain (MAG), which were extracted from the measured S-parameters of a device biased at a gate voltage of −2.8 V and a drain voltage of 10 V. The extra parasitic delays introduced by device probe pads were not de-embedded. The cut-off frequency (f_T) and maximum oscillation frequency (f_{max}) of 21 and 40 GHz, respectively, were extracted from $|h_{21}|^2$ and U, both of which exhibited the expected −20 dB/dec slope.

The DC and small-signal characteristics of the undoped XHEMTs with the same device dimensions are summarized in Figure S4 for comparison.

2.3 | Large-Signal RF Characteristics

In GaN-based HEMTs, devices exhibiting excellent DC and small-signal RF performance often fail to achieve high RF output power due to severe charge trapping effects, which lead to current collapse under RF operation conditions [30, 31]. Therefore, the extent and origins of charge trapping effects in newly designed heterostructures for HEMTs need to be carefully evaluated. A quick measurement to discern charge trapping is to observe whether the transistor channel current recovers fully or not when switching from off-state to on-state: charge trapping in any part of a transistor will prevent the transistor drain current to recover fully within a time period shorter than the charge de-trapping time. The ultimate test is to measure the transistor amplification performance as a function of the RF input signal

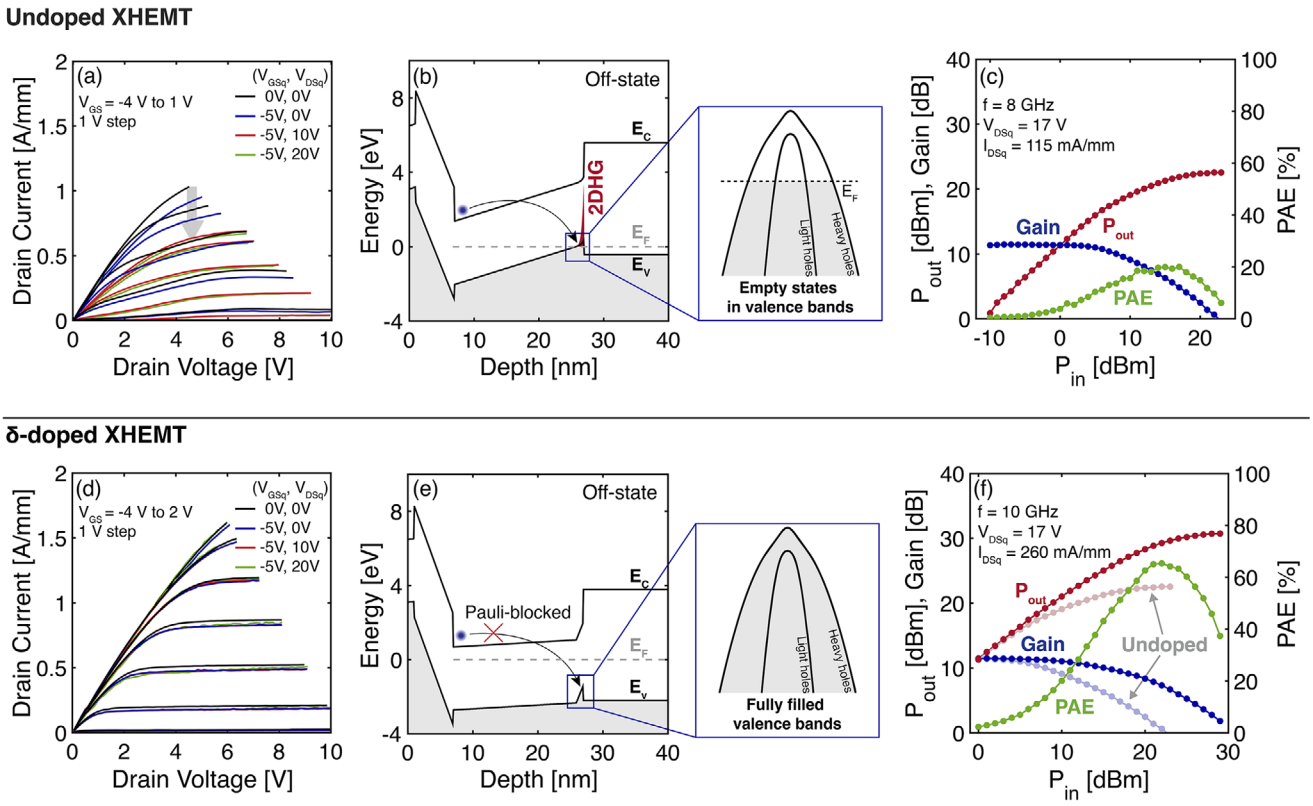

FIGURE 4 | Undoped (top row) vs δ-doped XHEMT (bottom row) on AlN, both fabricated using the same process flow. (a,d) Pulsed I_D-V_{DS} characteristics. Cold bias condition (V_{GSq}/V_{DSq} = 0 V/0 V) was used as a reference, and the applied stress bias conditions were V_{GSq}/V_{DSq} = −5V/0V, −5V/10V, and −5V/20V for both undoped and δ-doped XHEMTs. (b,e) Simulated energy band diagrams under the gate in the off-state. The undoped XHEMTs exhibited severe current collapse. We hypothesize when the transistor switches from on to off state, some electrons in the channel flow into the empty states in the valence band — i.e., holes — at the bottom GaN/AlN interface; however, these "trapped" electrons takes ms or longer to be fully released when the transistor switches back on, which leads to reduction in the mobile electrons in the channel therefore reduced drain current under pulsed bias conditions. On the other hand, δ-doped XHEMTs show negligible current collapse since these are no empty states in the valence band thanks to the electrons from the silicon donors. (c,f) CW load-pull power performance measurement as a function of input power, tuned for maximum PAE. In the undoped XHEMTs, the maximum P_{out} and peak PAE are limited to 0.90 W/mm and 20%, respectively, due to severe gain compression caused by electron trapping. In contrast, δ-doped XHEMTs exhibit a much higher maximum P_{out} of 5.92 W/mm and a peak PAE of 65%.

power so that the entire usable I–V area is accessed to amplify the RF signal: a transistor with minimal trapping should exhibit RF performance consistent with that predicted from the transistor DC I–V characteristics.

To this end, pulsed current-voltage ($I_D - V_{DS}$) measurements were applied to both the undoped and δ-doped XHEMTs using 300 nm long pulses at a 1 ms period to investigate their dynamic behavior under large-signal drive conditions. As shown in Figure 4a, the undoped XHEMTs show severe current collapse exceeding 30% under a stress bias condition of V_{GSq}, V_{DSq} = −5 V, 20 V, compared to the cold bias condition of V_{GSq}, V_{DSq} = 0 V, 0 V. In contrast, a dramatic improvement in trapping phenomena was achieved in δ-doped XHEMTs with silicon δ-doping. The δ-doped XHEMTs demonstrated negligible current collapse under the same stress bias condition of V_{GSq}, V_{DSq} = −5 V, 20 V, as shown in Figure 4d.

The large current collapse is consistently observed in surface-passivated undoped XHEMTs with varying device dimensions and different 2DEG densities ranging from 1.8×10^{13} cm^{-2} to 3.4×10^{13} cm^{-2} (thus corresponding maximum drain current densities) across multiple samples that were grown and processed independently. We attribute this current collapse partly to deep levels in the AlN buffer layer (yet to be verified) and partly to electrons being captured in empty states in the valence band at the bottom GaN/AlN interface (verified in this study), located approximately 20 nm below the 2DEG channel, as shown in the simulated off-state energy band diagram in Figure 4b. Once captured, these electrons are unable to return immediately to their original state, limited by the large time constant associated with thermalization of electrons from valence band to conduction band in (ultra)wide bandgap semiconductors as explained in our earlier article [32] and the n+GaN/2DHG contact at the bottom GaN/AlN interface, when the undoped XHEMT transitions back to its on-state during the positive cycle of the gate signal, leading to partial depletion of the 2DEG thus current collapse.

In the case of δ-doped XHEMTs, silicon δ-doping shifts the Fermi level closer to the midgap, effectively filling the valence band states. As a result, the capture of electrons is Pauli-blocked, as shown in the off-state energy band diagram in Figure 4e, preventing partial depletion of 2DEG. It is worth

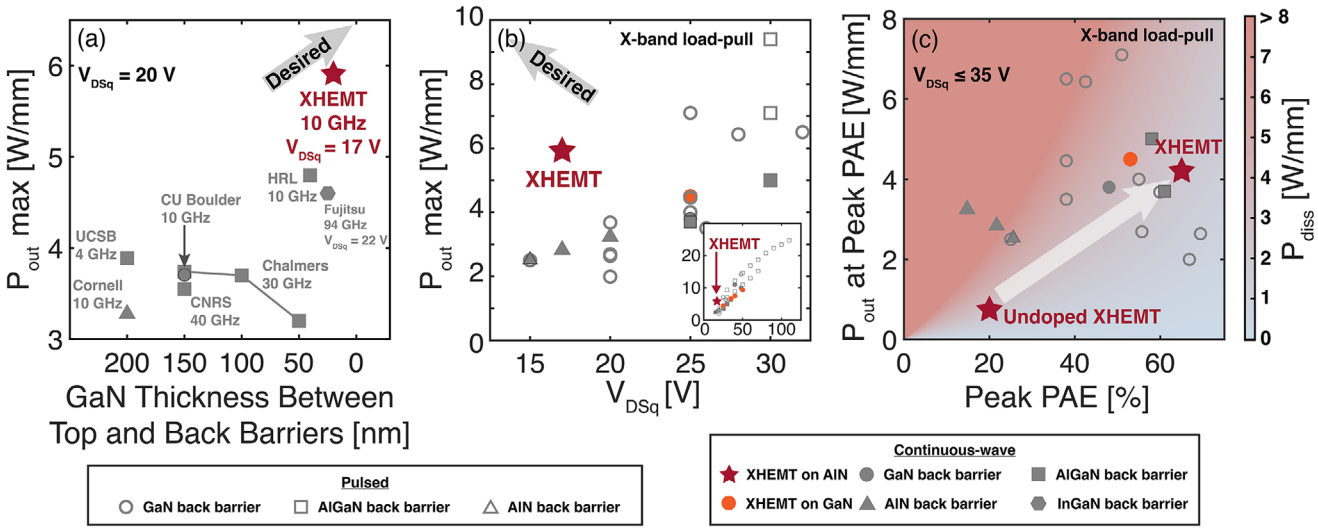

FIGURE 5 | Benchmarking δ-doped XHEMTs with metal-polar, single-channel nitride HEMTs on large signal RF power amplification. Hollow symbols are for pulsed and solid symbols for CW performance. (a) Maximum P_{out} measured at $V_{DSq} = 20$ V and GaN channel thickness (GaN thickness between the top and back barriers), in comparison to HEMTs with an AlN (triangle), AlGaN (square), GaN (circle), and InGaN (hexagon) back barrier reported in the literature [35–41]. Generally speaking, the conventional GaN back barrier is impurity doped with Fe or C, which possesses deep levels in GaN, and the GaN channel layer has a compensation doping concentration below 1×10^{17} cm^{-3}; accordingly, the GaN channel thickness is between 100 and 200 nm. (b) P_{out} as a function of V_{DSq}, comparison to previously reported HEMTs in X-band [41–58]. (c) Comparison of P_{out} at peak PAE versus peak PAE in X-band with $V_{DSq} \leq 35$ V. δ-doped XHEMTs shows significant improvements over the undoped XHEMTs, moving closer to the desired upper-right corner. In the context of thermal properties, only P_{out} values at peak PAE from Figure 4 are shown in this benchmark plot. The color map shows the dissipated power (P_{diss}) at a given P_{out} and PAE, derived under the assumption of 8 dB transducer power gain at peak PAE.

noting that studies yet need to be carried out to characterize electrical responses of deep levels in our homoepitaxial AlN buffer and their impact on XHEMTs; however, our earlier work using cryogenic temperature cathodoluminescence (CL) as a probe shows intense free exciton emission in our homoepitaxial AlN grown by MBE with suppression of near 3 - 4 eV emission due to deep levels as well as a total absence of prevalent donors that are present in bulk AlN substrates [33].

The continuous-wave (CW) large-signal performance of the undoped XHEMTs was investigated to confirm the charge trapping effects. The undoped XHEMT, biased at $V_{DSq} = 17$ V and $I_{DSq} = 0.115$ A/mm, demonstrated a maximum output power density (P_{out}) and a peak power-added efficiency (PAE) limited to 0.90 W/mm and 20%, respectively, at 8 GHz. These values fall far short of the expected P_{out} based on its output characteristics and bias point. As shown in Figure 4c, the P_{out} and PAE of undoped XHEMTs are constrained by the gain compression, caused by electron trapping, as anticipated from the previous pulsed I_D–V_{DS} measurements.

The CW large-signal measurements performed on δ-doped XHEMTs further confirmed the effectiveness of silicon δ-doping in suppressing RF dispersion. Biased at $V_{DSq} = 17$ V and $I_{DSq} = 0.26$ A/mm, δ-doped XHEMTs exhibited a maximum P_{out} of 5.92 W/mm and a peak PAE of 65%, as shown in Figure 4f when tuned for maximum PAE; under the same matching conditions, the associated P_{out} at the peak PAE was 4.2 W/mm. These results, enabled by silicon δ-doping, represent nearly sixfold and threefold increases in P_{out} and PAE, respectively, compared to the undoped XHEMT. Further increase in P_{out} is currently limited by the device breakdown voltage due to a non-optimized electric field management near the gate edge. The DC three-terminal breakdown characteristics of the δ-doped XHEMTs are shown in Figure S5. The influence of δ-doping on gate controllability and breakdown voltage remains under active investigation and represents an important direction for future work to further enhance device performance.

In previous studies, we reported that AlN/GaN/AlN HEMTs on bulk AlN substrates with a thick, relaxed 250-nm GaN layer exhibit low RF dispersion [5, 34]. This low dispersion is presently attributed to the large separation between the electron channel at the top AlN/GaN interface and empty states — if present and not compensated by other defects — in the valence band at the bottom GaN/AlN interface by the thick GaN layer. Furthermore, the thick GaN layer likely possesses compensating defects, which also hinder electrons from being captured in the empty states. This highlights a challenge in scaling the GaN channel thickness on AlN — the most suitable back barrier in terms of its high energy barrier to confine electrons, its atomically sharp isostructural interface with GaN, and its high thermal conductance. While increasing the channel thickness mitigates RF current collapse, a high density threading dislocation density is inevitable in a thick, relaxed GaN channel layer, which will negate the key advantages offered by the single crystal AlN substrate illustrated in Figure 1. Given that the pseudomorphic GaN thickness is about 20 nm on AlN due to their lattice mismatch, and that the 2DHG can develop in a pseudomorphic GaN on AlN as thin as 3 nm, it is essential to introduce donor doping to compensate the negative sheet charge at the bottom of the GaN/AlN interface.

Clearly, many aspects of the δ-doped XHEMTs should be improved and explored, including further reduction of the GaN channel thickness and mobile electron concentration under the gate while improving electron mobility, further increase in breakdown voltage, studies of device reliability, device-processing-circuit co-design to maximize the advantages that AlN offers, etc. However, the excellent RF performance achieved in these early generations of the δ-doped XHEMTs represents the first success toward developing active RF devices based on single-crystal AlN.

2.4 | Benchmarking

To evaluate the potential of δ-doped XHEMTs, we benchmark the large signal RF performance obtained on these first-generation δ-doped XHEMTs grown on Al-polar AlN against their counterpart: metal-polar, single-channel GaN HEMTs reported in the literature.

Figure 5a benchmarks the large-signal performance of δ-doped XHEMTs in terms of P_{out} as a function of GaN channel thickness (GaN thickness between the top and the bottom barrier). As the GaN channel thickness decreases, large-signal RF amplification becomes increasingly challenging due to factors such as mobility degradation and higher DC-RF dispersion [35]. By incorporating silicon δ-doping into the δ-doped XHEMT structure to overcome these challenges, this work reports the first large-signal operation of double-heterostructure HEMTs with a channel thickness at or below 20 nm. Moreover, the reported P_{out} is the highest achieved for V_{DSq} at or below 20 V among all metal-polar, single-channel GaN HEMTs though not all available data in the literature are at 10 GHz.

In Figure 5b, P_{out} of metal-polar, single-channel GaN HEMTs, including but not limited to double-heterostructure HEMTs, is plotted against V_{DSq} in the frequency range from 8 to 12 GHz. At a given V_{DSq}, δ-doped XHEMTs deliver significantly larger P_{out} compared to conventional AlGaN/GaN HEMTs, owing to their higher 2DEG density. The values used to create the benchmark figure are summarized in the supplementary material. While the δ-doped XHEMTs reported here exhibit state-of-the-art performance at moderate drain biases, previously published GaN devices operated at higher drain voltages have demonstrated output powers over 20 W/mm, as shown in the inset of Figure 5b. Because the present δ-doped XHEMTs are limited by the breakdown voltage, their performance under similar high-bias conditions cannot yet be evaluated. Improving breakdown strength will therefore be a key step toward realizing the full high-power potential of the δ-doped XHEMT architecture.

Lastly, Figure 5c shows the associated P_{out} at peak PAE of δ-doped XHEMTs compared with those of GaN HEMTs in Figure 5b, measured at V_{DSq} at or under 35 V in the X-band. A dramatic improvement in the large-signal RF performance of δ-doped XHEMTs is highlighted here, compared to the undoped XHEMT. When the problem of charge trapping thus RF dispersion is addressed in the δ-doped XHEMT, the HEMT performance on the AlN platform moves closer to the upper-right desired corner — which is for simultaneously higher P_{out} and PAE with a cooler device junction.

3 | Conclusion

In this study, we introduce XHEMTs on AlN, leveraging a thin pseudomorphic GaN channel sandwiched between AlN layers on single-crystal AlN substrates. The epitaxial layers in the XHEMT structure exhibit nearly a million-fold reduction in dislocation density compared to the conventional HEMT structure grown on foreign substrates, as well as the highest reported thermal boundary conductance at the growth interface among the material systems used in GaN HEMTs. We also show that silicon δ-doping, inserted at the bottom of the GaN channel enables dispersion-free operation by Pauli-blocking electron capture at the GaN/AlN interface where net negative polarization-bound charges are present, which would otherwise induce 2DHG leading to charge trapping thus dispersion. Experimental results confirm the potential of silicon δ-doped XHEMTs, demonstrating a maximum output power density of 5.92 W/mm and a peak power added efficiency of 65% at 10 GHz under a drain bias of 17 V. While further optimization of contact resistance and device design—particularly field management thus increasing the quiescent drain bias—is essential to achieve higher output power, these findings represent a significant milestone in the development of efficient RF electronics on the AlN platform that promises excellent thermal management and thin device layers by epitaxial growth.

4 | Experimental Section

4.1 | Epitaxial growth and electrical transport characterization

AlN XHEMT heterostructures were grown on single-crystal AlN substrates from Asahi-Kasei, with dislocation densities below 10^4 cm^{-2}. Epitaxial growth was performed using a Veeco GEN10 plasma-assisted molecular beam epitaxy (MBE) system, equipped with Al, Ga and Si standard effusion cells for metal flux control, as well as an RF plasma source for active nitrogen gas supply. Film growth was monitored in situ using a KSA Instruments reflection high-energy electron diffraction (RHEED) apparatus with a Staib electron gun operating at 14.5 kV and 1.45 A.

Following the cleaning process, a $\sim$ 500 nm AlN buffer layer was grown under metal-rich conditions at a thermocouple temperature of T_c = 1040°C, achieving step-flow growth mode. Excess Al droplets were desorbed in-situ by raising the substrate temperature by 50°C, with the desorption process monitored via RHEED intensity. The substrate was then cooled down to $T_c \sim$ 840°C for GaN channel growth.

The active region, consisting of a GaN channel layer, an AlN barrier, and a GaN cap, was grown continuously under metal-rich conditions without growth interruptions. An RF plasma power of 200 W and an N_2 gas flow of 0.35 sccm were maintained during active region growth, corresponding to a growth rate of 0.2 μm/h. In the δ- doped XHEMT, silicon δ-doping was incorporated after depositing 1 nm GaN. During the δ-doping step, we opened the silicon shutter while keeping the Ga and N shutters closed and the N2 plasma on for the time required to achieve a sheet density of $\sigma_\delta = 5 \times 10^{13}$ cm^{-2}. After completing the δ-doping process, we promptly reopened the Ga and N shutters to resume growth of

the remaining 19 nm GaN quantum well and subsequent layers. The δ-doping condition was calibrated using a separate MBE-grown silicon-doped GaN sample, with a silicon cell temperature of 1300°C, yielding a 3D doping density of 4.6×10^{19} cm^{-3}.

Upon completion of epitaxial growth, the substrate was cooled immediately to room temperature, and excess Ga droplets were removed ex situ using HCl. The growth of undoped XHEMTs followed the same procedure as that of δ-doped XHEMTs, except without the silicon δ-doping step. Following Ga droplet removal, a Nanometrics Hall system was used to measure electron mobility and 2DEG density in the as-grown samples using soldered indium corner contacts to the 2DEG.

4.2 | Device Fabrication

Device fabrication began with patterning the sample for source and drain ohmic contact definition. SiO_2 and Cr hard masks were blanket-deposited on a 1×1 cm^2 δ-doped XHEMT sample via low-power PECVD and electron-beam evaporation, respectively. The sample was then patterned using photolithography. Cr in the open contact windows was removed via O_2/Cl_2 ICP etching, and SiO_2 was etched using CF_4/CHF_3 reactive ion etching (RIE), with the patterned Cr serving as a hard mask after the photoresist was removed. The 2DEG sidewall was subsequently exposed by BCl_3 ICP etch, which extended approximately 10 nm into the AlN back barrier. The Cr layer was removed using a ceric ammonium nitrate-based wet etchant, and the SiO_2 hard mask was laterally recessed into the access region by approximately 80 nm using a diluted buffered oxide etchant (BOE). The patterned sample was loaded into a molecular beam epitaxy chamber, where a 60-nm thick n+ GaN layer was regrown.

The regrown n+ GaN outside the source and drain regions was lifted off using BOE, and devices were mesa-isolated by a BCl_3 ICP etch that extended into the AlN back barrier. Surface-passivation was then performed by depositing 106-nm thick near stoichiometric SiN_x in a LPCVD chamber at a thermocouple temperature of 750°C. Dichlorosilane and ammonia precursors were used to grow near stoichiometric SiN_x. Non-alloyed source and drain ohmic contacts were then metallized by patterning the sample via photolithography, followed by SiN_x removal using CHF_3/O_2 RIE and electron-beam evaporation of Ti/Au = 40/100 nm.

Gate stems were defined by a 100 keV JEOL 6300 electron beam lithography (EBL) system, followed by a gate recess etch performed via low-power SF_6 ICP etch to form Schottky contacts on GaN. The head width of T-shaped gates was defined using the same EBL system, and gates were metallized by electron-beam evaporation of Ni/Au = 40/350 nm. For RF measurements, coplanar waveguide bonding pads were connected to the transistor electrodes through electron-beam evaporating Ti/Au = 40/360 nm on a sample patterned via photolithography. A 116 nm-thick SiN_x layer was then blanket deposited using PECVD. The sample was subsequently patterned by photolithography and SiN_x on the transistor electrodes was removed via CHF_3/O_2 RIE to facilitate probing for electrical measurements. Lastly, SCFPs were defined using EBL and metallized by electron-beam evaporation of Ti/Au = 40/400 nm.

4.3 | DC and RF Characterization

The capacitance–voltage, and pulsed current–voltage characteristics of the HEMTs were measured using a Cascade Microtech Summit 11000 probe system and a Keithley 4200A-SCS parameter analyzer. Small-signal RF characterization was performed by measuring scattering using an Agilent E8364B vector network analyzer, with the DC bias supplied by an Agilent 4156C parameter analyzer. The transfer and output characteristics of the HEMTs were measured using the same system. The measurements were calibrated using short, open, load, and through impedance standards with Infinity ground–signal–ground (GSG) probes. The large-signal RF characterization was performed using a Maury Microwave MT2000 mixed signal active load-pull system with Infinity GSG probes. The optimum load and source reflection coefficients, tuned for maximum PAE, were Γ_L = 0.23+0.32i and Γ_S = -0.68+0.37i, respectively, for the δ-doped XHEMT, and Γ_L = 0.72+0.35i and Γ_S = -0.69+0.35i, respectively, for the undoped XHEMT.

4.4 | Electron Microscopy

A cross-section lamella was prepared using the Thermo Fisher Helios G4 UX Focused Ion Beam. Protective C and Pt layers were deposited on the lamella and prepared with a final milling step of 5 keV to reduce damage. Scanning transmission electron microscopy (STEM) measurements were taken with an aberration-corrected Thermo Fisher Spectra 300 CFEG operated at 300 keV.

Acknowledgements

This work was supported in part by ARO (device conceptualization, epitaxy, demonstration and characterization), under Grant No. W911NF-22-2-0177, by DARPA THREADS program (X-band device fabrication and characterization), Asahi-Kasei Corporation (substrates and epitaxy), and performed at the Cornell Nanoscale Facility, an NNCI member supported by NSF Grant No. NNCI-2025233. This work made use of the electron microscopy facility of the Cornell Center for Materials Research (CCMR) with support from the National Science Foundation Materials Research Science and Engineering Centers (MRSEC) program (DMR1719875). The Thermo Fisher Spectra 300 X-CFEG was acquired with support from PARADIM, an NSF MIP (DMR-2039380) and Cornell University. E.K. and N.P. acknowledge support from National Science Foundation Graduate Research Fellowship under Grant No. DGE2139899.

Conflicts of Interest

The authors declare no conflicts of interest.

Data Availability Statement

The data that support the findings of this study are available from the corresponding author upon reasonable request.

References

1. R. T. Bondokov, K. Hogan, G. Q. Norbury, S. Matsumoto, and J. Grandusky, "Development of 100 mm AlN Single-Crystal Growth and Subsequent Substrate Preparation," *Physica Status Solidi (b)* (2025): 2500032, https://onlinelibrary.wiley.com/doi/abs/10.1002/pssb.202500032.

2. R. T. Bondokov, S. P. Branagan, N. Ishigami, et al., "Two-Inch Aluminum Nitride (AlN) Single Crystal Growth for Commercial Applications," *ECS Meeting Abstracts* MA2021-02, no. 34 (2021): 985, https://dx.doi.org/10.1149/MA2021-0234985mtgabs.

3. Z. Zhang, M. Kushimoto, T. Sakai, et al., "A 271.8 nm Deep-Ultraviolet Laser Diode for Room Temperature Operation," *Applied Physics Express* 12, no. 12 (2019): 124003, https://dx.doi.org/10.7567/1882-0786/ab50e0.

4. R. Rounds, B. Sarkar, A. Klump, et al., "Thermal Conductivity of Single-Crystalline AlN," *Applied Physics Express* 11, no. 7 (2018): 071001, https://dx.doi.org/10.7567/APEX.11.071001.

5. Y.-H. Chen, J. Encomendero, C. Savant, V. Protasenko, H. G. Xing, and D. Jena, "Electron Mobility Enhancement by Electric Field Engineering of AlN/GaN/AlN Quantum-Well HEMTs on Single-Crystal AlN Substrates," *Applied Physics Letters* 124, no. 15 (2024): 152111, https://doi.org/10.1063/5.0190822.

6. Y.-H. Chen, J. Encomendero, C. Savant, V. Protasenko, H. G. Xing, and D. Jena, "High Conductivity Coherently Strained Quantum Well XHEMT Heterostructures on AlN Substrates with Delta Doping," *Applied Physics Letters* 125, no. 14 (2024): 142110, https://doi.org/10.1063/5.0228253.

7. M. Qi, G. Li, S. Ganguly, et al., "Strained GaN Quantum-Well FETs on Single Crystal Bulk AlN Substrates," *Applied Physics Letters* 110, no. 6 (2017): 063501, https://doi.org/10.1063/1.4975702.

8. Z. Zhang, J. Encomendero, R. Chaudhuri, et al., "Polarization-Induced 2D Hole Gases in Pseudomorphic Undoped GaN/AlN Heterostructures on Single-Crystal AlN Substrates," *Applied Physics Letters* 119, no. 16 (2021): 162104, https://doi.org/10.1063/5.0066072.

9. K. J. Chen, O. Häberlen, A. Lidow, et al., "GaN-on-Si Power Technology: Devices and Applications," *IEEE Transactions on Electron Devices* 64, no. 3 (2017): 779–795.

10. Y. Tang, K. Shinohara, D. Regan, et al., "Ultrahigh-Speed GaN High-Electron-Mobility Transistors with $f_T/f_{\max}$ of 454/444 GHz," *IEEE Electron Device Letters* 36, no. 6 (2015): 549–551.

11. K. M. Bothe, S. Ganguly, J. Guo, et al., "Improved X-Band Performance and Reliability of a GaN HEMT with Sunken Source Connected Field Plate Design," *IEEE Electron Device Letters* 43, no. 3 (2022): 354–357.

12. H. Ishikawa, G.-Y. Zhao, N. Nakada, T. Egawa, T. Jimbo, and M. Umeno, "GaN on Si Substrate with AlGaN/AlN Intermediate Layer," *Japanese Journal of Applied Physics* 38, no. 5A (1999): L492, https://dx.doi.org/10.1143/JJAP.38.L492.

13. S. Lawrence Selvaraj, T. Suzue, and T. Egawa, "Breakdown Enhancement of AlGaN/GaN HEMTs on 4-in Silicon by Improving the GaN Quality on Thick Buffer Layers," *IEEE Electron Device Letters* 30, no. 6 (2009): 587–589.

14. M. J. Uren, J. Moreke, and M. Kuball, "Buffer Design to Minimize Current Collapse in GaN/AlGaN HFETs," *IEEE Transactions on Electron Devices* 59, no. 12 (2012): 3327–3333.

15. M. Meneghini, I. Rossetto, D. Bisi, et al., "Buffer Traps in Fe-Doped AlGaN/GaN HEMTs: Investigation of the Physical Properties Based on Pulsed and Transient Measurements," *IEEE Transactions on Electron Devices* 61, no. 12 (2014): 4070–4077.

16. A. Sarua, H. Ji, K. P. Hilton, et al., "Thermal Boundary Resistance between GaN and Substrate in AlGaN/GaN Electronic Devices," *IEEE Transactions on Electron Devices* 54, no. 12 (2007): 3152–3158.

17. R. L. Coffie, "High Power High Frequency Transistors: A Material's Perspective," *High-Frequency GaN Electronic Devices* (2019), https://api.semanticscholar.org/CorpusID:201295319.

18. A. Manoi, J. W. Pomeroy, N. Killat, and M. Kuball, "Benchmarking of Thermal Boundary Resistance in AlGaN/GaN HEMTs on SiC Substrates: Implications of the Nucleation Layer Microstructure," *IEEE Electron Device Letters* 31, no. 12 (2010): 1395–1397.

19. S. G. Mueller, R. T. Bondokov, K. E. Morgan, et al., "The Progress of AlN Bulk Growth and Epitaxy for Electronic Applications," *Physica Status Solidi (a)* 206, no. 6 (2009): 1153–1159, https://onlinelibrary.wiley.com/doi/abs/10.1002/pssa.200880758.

20. E. Kim, Z. Zhang, J. Encomendero, et al., "N-polar GaN/AlGaN/AlN High Electron Mobility Transistors on Single-Crystal Bulk AlN Substrates," *Applied Physics Letters* 122, no. 9 (2023): 092104, https://doi.org/10.1063/5.0138939.

21. G. Alvarez-Escalante, R. Page, R. Hu, H. G. Xing, D. Jena, and Z. Tian, "High Thermal Conductivity and Ultrahigh Thermal Boundary Conductance of Homoepitaxial AlN Thin Films," *APL Materials* 10, no. 1 (2022): 011115, https://doi.org/10.1063/5.0078155.

22. Y. Cao and D. Jena, "High-Mobility Window for Two-Dimensional Electron Gases at Ultrathin AlN/GaN Heterojunctions," *Applied Physics Letters* 90, no. 18 (2007): 182112, https://doi.org/10.1063/1.2736207.

23. P. Döring, S. Krause, C. Friesicke, and R. Quay, "Theoretical Limits of the Matching Bandwidth and Output Power of AlScN-Based HEMTs," *IEEE Transactions on Electron Devices* 71, no. 3 (2024): 1670–1675.

24. W. Wang, X. Yu, J. Zhou, et al., "Improvement of Power Performance of GaN HEMT by Using Quaternary InAlGaN Barrier," *IEEE Journal of the Electron Devices Society* 6 (2018): 360–364.

25. C. F. C. Chang, J. E. Dill, Z. Zhang, et al., "Quantum Oscillations of Holes in GaN," (2025).

26. R. Chaudhuri, S. J. Bader, Z. Chen, D. A. Muller, H. G. Xing, and D. Jena, "A Polarization-Induced 2D Hole Gas in Undoped Gallium Nitride Quantum Wells," *Science* 365, no. 6460 (2019): 1454–1457, https://www.science.org/doi/abs/10.1126/science.aau8623.

27. Y.-H. Chen, J. Encomendero, C. F. C. Chang, H. G. Xing, and D. Jena, "Shubnikov–de Haas oscillations of 2DEGs in Coherently Strained AlN/GaN/AlN Heterostructures on Bulk AlN Substrates," *Applied Physics Letters* 126, no. 20 (2025): 202101, https://doi.org/10.1063/5.0264000.

28. J. E. Dill, C. F. C. Chang, D. Jena, and H. G. Xing, "Two-Carrier Model-Fitting of Hall Effect in Semiconductors with Dual-Band Occupation: A Case Study in GaN Two-Dimensional Hole Gas," *Journal of Applied Physics* 137, no. 2 (2025): 025702, https://doi.org/10.1063/5.0248998.

29. H. Amano, M. Kito, K. Hiramatsu, and I. Akasaki, "P-Type Conduction in Mg-Doped GaN Treated with Low-Energy Electron Beam Irradiation (LEEBI)," *Japanese Journal of Applied Physics* 28, no. 12A (1989), L2112, https://dx.doi.org/10.1143/JJAP.28.L2112.

30. S. Binari, K. Ikossi, J. Roussos, et al., "Trapping Effects and Microwave Power Performance in AlGaN/GaN HEMTs," *IEEE Transactions on Electron Devices* 48, no. 3 (2001): 465–471.

31. R. Vetury, N. Zhang, S. Keller, and U. Mishra, "The Impact of Surface States on the DC and RF Characteristics of AlGaN/GaN HFETs," *IEEE Transactions on Electron Devices* 48, no. 3 (2001): 560–566.

32. W. Li, Z. Hu, K. Nomoto, D. Jena, and H. G. Xing, *Unleashing the Promise of Gallium Oxide* (Compound Semiconductor 2019).

33. L. van Deurzen, J. Singhal, J. Encomendero, et al., "Excitonic and Deep-Level Emission from N- and Al-Polar Homoepitaxial AlN Grown by Molecular Beam Epitaxy," *APL Materials* 11, no. 8 (2023): 081109, https://doi.org/10.1063/5.0158390.

34. E. Kim, Y.-H. Chen, J. Encomendero, D. Jena, and H. G. Xing, "AlN/GaN/AlN HEMTs on Bulk AlN Substrates with High Drain Current Density > 2.8 A/mm and Average Breakdown Field > 2 MV/cm," in *2024 Device Research Conference (DRC)* (2024), 1–2.

35. A. Malmros, P. Gamarra, M. Thorsell, et al., "Impact of Channel Thickness on the Large-Signal Performance in InAlGaN/AlN/GaN HEMTs with an AlGaN Back Barrier," *IEEE Transactions on Electron Devices* 66, no. 1 (2019): 364–371.

36. K. Harrouche, S. Venkatachalam, L. Ben-Hammou, F. Grandpierron, E. Okada, and F. Medjdoub, "Low Trapping Effects and High Electron Confinement in Short AlN/GaN-on-SiC HEMTs by Means of a Thin AlGaN Back Barrier," *Micromachines* 14, no. 2 (2023), https://www.mdpi.com/2072-666X/14/2/291.

37. S. Kaun, M. Wong, J. Lu, U. Mishra, and J. Speck, "Reduction of Carbon Proximity Effects by Including AlGaN Back Barriers in HEMTs on Free-Standing GaN," *Electronics Letters* 49, no. 14 (2013): 893–895, https://ietresearch.onlinelibrary.wiley.com/doi/abs/10.1049/el.2013.1723.

38. A. Hickman, R. Chaudhuri, L. Li, et al., "First RF Power Operation of AlN/GaN/AlN HEMTs with >3 A/mm and 3 W/mm at 10 GHz," *IEEE Journal of the Electron Devices Society* 9 (2021): 121–124.

39. J. Kotani, K. Makiyama, T. Ohki, et al., "High-Power-Density InAlGaN/GaN HEMT using InGaN Back Barrier for W-Band Amplifiers," *Electronics Letters* 59, no. 4 (2023): e12715, https://ietresearch.onlinelibrary.wiley.com/doi/abs/10.1049/ell2.12715.

40. M. Micovic, P. Hashimoto, M. Hu, et al., "GaN Double Heterojunction Field Effect Transistor for Microwave and Millimeterwave Power Applications," in *IEDM Technical Digest. IEEE International Electron Devices Meeting, 2004.* (2004), 807–810.

41. S. Schafer, M. Litchfield, A. Zai, Z. Popovíc, and C. Campbell, "X-Band MMIC GaN Power Amplifiers Designed for High-efficiency supply-modulated transmitters," in *2013 IEEE MTT-S International Microwave Symposium Digest (MTT)* (2013), 1–3.

42. D. Sardin, T. Reveyrand, and Z. Popović, "X-Band 10W MMIC High-Gain Power Amplifier with up to 60% PAE," in *2014 44th European Microwave Conference* (2014), 1337–1340.

43. C. Lee, P. Saunier, and H.-Q. Tserng, "High-Temperature Power Performance of X-Band Recessed-Gate AlGaN/GaN HEMTs," in *IEEE Compound Semiconductor Integrated Circuit Symposium, 2005. CSIC '05.* (2005), 157–160.

44. P.-C. Chao, K. Chu, C. Creamer, et al., "Low-Temperature Bonded GaN-on-Diamond HEMTs with 11 W/mm Output Power at 10 GHz," *IEEE Transactions on Electron Devices* 62, no. 11 (2015): 3658–3664.

45. Y.-F. Wu, A. Saxler, M. Moore, et al., "30-W/mm GaN HEMTs by Field Plate Optimization," *IEEE Electron Device Letters* 25, no. 3 (2004): 117–119.

46. X. Luo, S. Halder, W. R. Curtice, et al., "Scaling and High-Frequency Performance of AlN/GaN HEMTs," in *2011 IEEE International Symposium on Radio-Frequency Integration Technology* (2011), 209–212.

47. M. Peng, Y. Zheng, W. Luo, and X. Liu, "14.2 W/mm Internally-Matched AlGaN/GaN HEMT for X-Band Applications," *Solid-State Electronics* 64, no. 1 (2011): 63–66, https://www.sciencedirect.com/science/article/pii/S003811011100267X.

48. H.-Q. Tao, W. Hong, B. Zhang, and X.-M. Yu, "A Compact 60W X-Band GaN HEMT Power Amplifier MMIC," *IEEE Microwave and Wireless Components Letters* 27, no. 1 (2017): 73–75.

49. D. Resca, A. Raffo, S. Di Falco, F. Scappaviva, V. Vadalà, and G. Vannini, "X-Band GaN Power Amplifier for Future Generation SAR Systems," *IEEE Microwave and Wireless Components Letters* 24, no. 4 (2014): 266–268.

50. S. Piotrowicz, Z. Ouarch, E. Chartier, et al., "43W, 52% PAE X-band AlGaN/GaN HEMTs MMIC Amplifiers," in *2010 IEEE MTT-S International Microwave Symposium* (2010), 505–508.

51. S. Piotrowicz, E. Morvan, R. Aubry, et al., "State of the Art 58W, 38% PAE X-Band AlGaN/GaN HEMTs Microstrip MMIC Amplifiers," in *2008 IEEE Compound Semiconductor Integrated Circuits Symposium* (2008), 1–4.

52. K. Chu, P. Chao, M. Pizzella, et al., "9.4-W/mm Power Density AlGaN-GaN HEMTs on Free-Standing GaN Substrates," *IEEE Electron Device Letters* 25, no. 9 (2004): 596–598.

53. J. S. Moon, H. Moyer, P. Macdonald, et al., "High Efficiency X-Band Class-E GaN MMIC High-Power Amplifiers," in *2012 IEEE Topical Conference on Power Amplifiers for Wireless and Radio Applications* (2012), 9–12.

54. S. Ozaki, J. Yaita, A. Yamada, et al., "First Demonstration of X-Band AlGaN/GaN High Electron Mobility Transistors Using Free-Standing AlN Substrate Over 15 W · mm^{-1} Output Power Density," *Applied Physics Express* 14, no. 4 (2021): 041004, https://dx.doi.org/10.35848/1882-0786/abec90.

55. J. Kotani, J. Yaita, K. Homma, et al., "24.4 W/mm X-band GaN HEMTs on AlN Substrates with the LPCVD-Grown High-Breakdown-Field SiN_x Layer," *IEEE Journal of the Electron Devices Society* 11 (2023): 101–106.

56. Y. Pei, R. Chu, N. A. Fichtenbaum, et al., "Recessed Slant Gate AlGaN/GaN High Electron Mobility Transistors with 20.9 W/mm at 10 GHz," *Japanese Journal of Applied Physics* 46, no. 12L (nov 2007): L1087, https://dx.doi.org/10.1143/JJAP.46.L1087.

57. Y.-F. Wu, D. Kapolnek, J. Ibbetson, et al., "High Al-Content AlGaN/GaN HEMTs on SiC Substrates with Very High Power Performance," in *International Electron Devices Meeting 1999. Technical Digest (Cat. No.99CH36318)* (1999), 925–927.

58. Y.-F. Wu, D. Kapolnek, J. Ibbetson, P. Parikh, B. Keller, and U. Mishra, "Very-High Power ensity AlGaN/GaN HEMTs," *IEEE Transactions on Electron Devices* 48, no. 3 (2001): 586–590.

Supporting Information

Additional supporting information can be found online in the Supporting Information section.

Supporting Information